Lab on a Chip

Digital Microfluidic Meter-on-chip

Journal:	*Lab on a Chip*
Manuscript ID	LC-ART-10-2019-000989.R1
Article Type:	Paper
Date Submitted by the Author:	04-Dec-2019
Complete List of Authors:	Fang, Zecong; University of California Davis, Biomedical Engineering Ding, Yi; University of California Davis, Biomedical Engineering; University of California Davis, Electrical and Computer Engineering Zhang, Zhichao; University of California Davis, Biomedical Engineering Wang, Fei; Southern University of Science and Technology, School of Microelectronics Wang, Zuankai; City University of Hong Kong, Department of Mechanical Engineering Wang, Hao; Peking University, Department of Energy and Resources Engineering Pan, Tingrui; University of California Davis, Biomedical Engineering; University of California Davis, Electrical and Computer Engineering

ARTICLE

Digital Microfluidic Meter-on-chip

Zecong Fang [a], Yi Ding [ab], Zhichao Zhang [a], Fei Wang [c], Zuankai Wang [d], Hao Wang [e] and Tingrui Pan [*ab]

Received 00th January 20xx,
Accepted 00th January 20xx

DOI: 10.1039/x0xx00000x

Accurate monitoring and control of liquid flow at low flowrates becomes increasingly important in contemporary biomedical research and industrial monitoring. Inspired by the drop-counting principle implemented in the clinical gravity drip, we have proposed a novel microfluidic flowmetry technology for PDMS-based conventional microfluidic devices, known as microfluidic digital meter-on-chip (DMC), to achieve on-chip and localized microflow measurement with ultrahigh precision and wide tunable range. The DMC technology is primarily relied on capillarity, unlike gravity drip, to induce a characteristic interfacial droplet pinch-off process, from which the digital microflowmetry devices can discretize continuous flow into countable transferred liquid units with consistent quantifiable volumes. Enabled by the passive discretization principle and optical transparency, the DMC devices require no external energy input and bulky control equipment, and a non-contact wireless optical detection scheme using a smartphone can be conveniently used as the readout module. Moreover, the DMC technology has achieved an ultrahigh flow-to-frequency sensitivity (6.59 Hz/(µL/min)) and resolution (droplet transfer volume down to 2.5 nL, nearly two orders of magnitude smaller than the previous reported work that targets at ultralow flowrates at magnitude of 1 µL/min). In addition, the flowrate measurement range covers up to 80 µL/min and down to at least 150 nL/min (over 100 times smaller than the reported similar digital flowmetry at the same time scale) under the current device configuration. Benefiting from its simple device architecture and adaptability, the versatile DMC technology can be seamlessly integratable with various microfluidic and nanofluidic devices for drug delivery and biochemical analysis, serving as a promising platform technology for the next-generation high-demanding microflow measurement.

Introduction

Accurate monitoring and control of liquid flow at low flowrates becomes increasingly important in contemporary biomedical research and industrial monitoring. In particular, the drug delivery devices intend to incorporate in-line monitoring of flow as both precision enhancement and a safety feature. For instance, reliable flow measurement is highly demanded in a wide variety of medical devices, such as infusion pumps[1,2], implantable drug delivery devices[3], microdialysis tubes[4], and so on. Existing microflowmetry devices can be basically classified as thermal or non-thermal schemes based on their operational principles.[5–7] Thermal flowmeters, particularly those based on calorimetric sensing mechanism, are among the most commonly used flow sensors for low flowrate measurement, due to their structural and electronic simplicity.[5] Calorimetric thermal flow sensors typically contain both heating and temperature-sensing elements and flowrate can be correlated with the asymmetry in temperature profile around the heater. However, multiple drawbacks are present in thermal flowmeters. For example, its nonlinearity over the temperature range requires additional calibration steps and compensation designs.[6] It is also highly subject to fluidic contamination[6] and complexed flow (e.g., non-Newtonian). More severely, it may cause damages or changes of properties of the measured fluids, such as those containing biomolecules[8] due to the undesirable heating process and it can be susceptible to the variations in environment temperature[9,10]. On the other hand, an array of non-thermal flow sensors has been investigated for low flowrate measurement with various detection principles such as deflection of a cantilever[11–13], Coriolis force[14–17], differential pressure[18,19], electrical admittance[20], time-of-flight measurements of tracer chemicals[21] or heat pulses[22,23] (sometimes classified into the thermal-based category), deflection of a membrane[24], etc., with a range of different sensing and readout mechanisms such as optical deflection, electrical impedance, resonant frequency, etc. Unfortunately, these non-thermal flow sensors require either complicated device structures with less reliable fabrication processes[11] or extended external setups to function[25]. So far, none of them stays competitive with the aforementioned thermal-measuring standard in flow-sensing performance.[7]

Advent of microfluidic technology has attracted steadily increasing interest and become an important toolset of research and development for manipulating a variety of liquid substances at a miniature scale over past decades.[26,27] Microfluidics holds enormous potential to transform cumbersome laboratory operations by

---

[a] *Micro-Nano Innovations (MiNI) Laboratory, Department of Biomedical Engineering, University of California, Davis, CA, 95616, USA. E-mail: tingrui@ucdavis.edu*

[b] *Department of Electrical and Computer Engineering, University of California, Davis, CA, 95616, USA.*

[c] *School of Microelectronics, Southern University of Science and Technology, Shenzhen, 518055, China.*

[d] *Department of Mechanical Engineering, City University of Hong Kong, Hong Kong, 999077, China.*

[e] *Department of Energy and Resources Engineering, Peking University, Beijing, 100871, China.*

†Electronic Supplementary Information (ESI) available: [details of any supplementary information available should be included here. See DOI: 10.1039/x0xx00000x.

enabling chemical and biological analyses using a minute amount of reagents in a significantly reduced reaction time, with a growing number of applications ranging from point-of-care diagnosis, organ-on-chip, to synthetic biology.[28] As the key components, micropumps, microvalves and microfluidic sensors have played important roles in microfluidic devices. However, unlike the popularity in integrated micropump and microvalve research, the studies focused on on-chip microflow sensors have been limited in the existing literature.[5–7,29–33] On the other hand, the precise flow assessment in emerging microfluidic devices has been of critical importance in applications such as flow cytometry[34], particle sorting[35], flow mixing[36], emulsion generation[37], chemical and pharmaceutical production[38], and operation of microfluidic fuel cells[39]. For instance, in flow focusing devices, the flowrates of the continuous sheath and dispersed core flows have to be carefully maintained for generating consistently monodisperse droplets.[40,41] Besides, hydrodynamic force-enabled particle sorting/separation and flow cytometry are highly sensitive to the flowrate variation within the microfluidic channels.[34,35]

Nonetheless, the development of on-chip microfluidic flow sensors remains challenging, partly due to the difficulty of embedding the flow-sensing elements into the device structure, primarily made of polydimethylsiloxane (PDMS) elastomer. Though the conventional thermal flow sensors have impressive performance, the embedded electrodes and metallic thermistors are inherently difficult to be integrated into the PDMS devices, in addition to their complicated multi-layer patterning process[7]. Recently, several research attempts have been made by using non-thermal principles to achieve on-chip flow measurement in PDMS microfluidics. These efforts, primarily relied on mechanical deformation of a moving part in response to the flow, include measuring deflection of a PDMS cantilever[10], evaluating elongation of a stretchable spring-like structure[42], assessing rotation of a water-drop-shaped indicator[43] as well as determining changes in resonant frequency of a microwave resonator correlated with the deformation of a PDMS membrane[24]. Though these integrated designs can achieve proposed on-chip and local flow measurements in conventional PDMS microfluidics, they are either difficult to fabricate or added system complexity by incorporating moving parts or complex detection equipment. Therefore, innovations of microfluidic flow sensors that can measure on-chip and local flowrates with simple configuration, high precision, and direct adaptability with PDMS microstructures are still highly sought-after[24].

Inspired by the widely used gravity drip in clinic[44], our group has previously introduced a new microflow measurement principle, referred to as digital droplet flowmetry (DDF)[45], by discretizing a continuous flow into individual "digital" droplets using surface tension and capillarity instead. It has originally been implemented on an open-surface textile platform for in situ perspiration measurements with a single μL scale volume resolution in the range between 3.3μL/min and 67μL/min. The novel digitalized measurement principle provides promising features such as fast response, digital readouts, system flexibility, in addition to high precision. A later study from Gomez group[46] has applied the same principle to fabricate a digital flow dispensing system with a smaller transferred volume (of 128nL) and an expanded measuring range (of 25nL/min to 900μL/min). By improving the evaporation and movement control, the digital flow sensor has also targeted at a similar application of real-time perspiration monitoring. Another follow-up study from Li group[47] has implemented a similar geometrical configuration as Gomez group but with rather finely controlled fabrication process, using femtosecond laser direct-writing technology to prepare the droplet-generating nozzle and a Janus porous membrane for droplet absorption and removal. Flowrates ranging from 10μL/min to 200μL/min have been successfully measured and the smallest droplet transfer volume of 3.15nL has been achieved. Although these works have shown the great potential of digital flowmetry in microflow measurement, the proposed flowmeters both have been configured in a three-dimensional architecture with an open-air interface, which implies

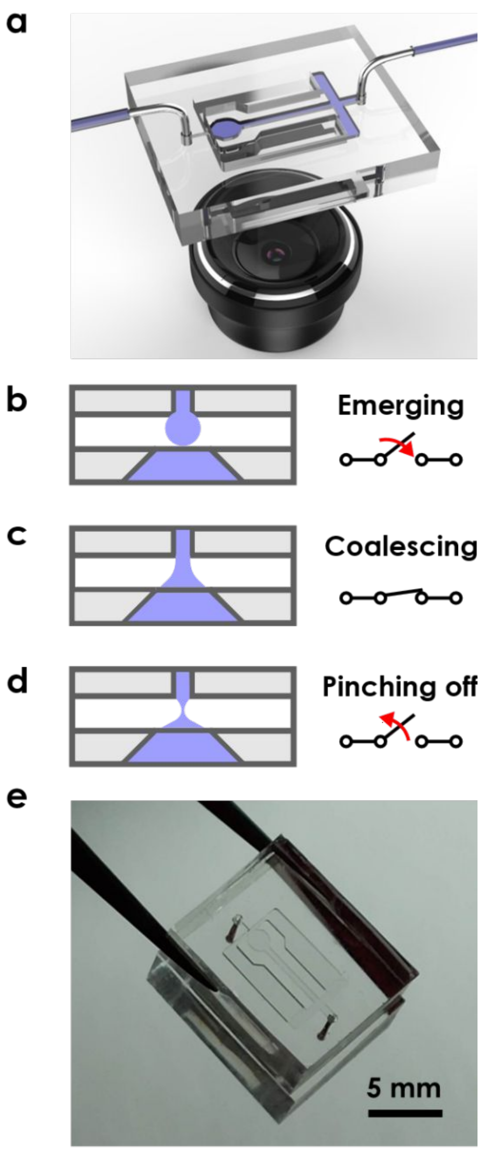

Fig. 1 The microfluidic digital meter-on-chip (DMC) concept. a) Illustration of the DMC concept with an optical detection scheme in addition to b-d) Illustration of the periodic formation (equivalent to closed-loop circuit) and breakup (equivalent to open-loop circuit) of a liquid bridge, e) Prototype of a DMC device.

digital flowmetry has not yet been readily implemented for standard microfluidic integration with its planar and enclosed architecture.

In this study, we have proposed and achieved the first on-chip digital flow-measuring device with simple non-contact readout mechanisms, referred to as digital meter-on-chip (DMC), utilizing the aforementioned digital microflowmetry principle, which is completely compatible with the standard fabrication steps of the PDMS-based microfluidic devices and can be easily incorporated into any existing microfluidic designs. The simple device architecture of the digital flowmeter permits the digitization of the flow governed by capillarity without external energy required. Remarkably, as its name indicates, the output signals of the DMC are simply digital or the counts of microfluidic discretization, and therefore, we have adopted two straightforward readout schemes, that is, non-contact directly optical readout (e.g., by a smartphone camera) and wired electrical detection (allowing high-speed counting). It is worth noting that such a two-dimensional flowmeter can measure flowrates ranging from hundreds of nL/min to tens of μL/min, with a single droplet transfer volume down to 2.5nL, of which the sensitivity is at least 50 times greater than that of the prior art that targets at 1μL/min scale flowrates[45–47]. To demonstrate the utility of the DMC for on-chip flowrate monitoring, an array of DMC devices has been successfully integrated into a classic microfluidic Christmas-tree-like gradient generator to detect the flowrate distribution in each channel, both when the two inlets have the same and different flowrates, respectively.

Operating Principle

In principle, the digital flowmetry assesses flowrate by discretizing continuous flow into "digital" and consistent droplets using capillarity, analogous to the classic gravity drip used in clinic settings[48,49]. As a result, the volumetric flowrate (Q) can be correlated directly with the frequency of digitization (f) and the droplet transfer volume (V_t), as $Q = f \cdot V_\mathrm{t}$. As expected, to ensure the measurement accuracy in the digital flowmetry, it is important to decouple the correlations between the droplet transfer volume and the flowrate variations during the process of "analog-to-digital" conversion. Unlike the gravity drips that utilize gravitational force, herein we take the advantages of surface tension force for discretization in digital flowmetry, which considerably overwhelms the inertial and gravitational forces under the capillary length, and primarily depends on the microfluidic geometries (e.g., channel and nozzle dimensions)[50]. Therefore, within a low flowrate range (when Weber number $We = \rho u^2 R/\sigma \ll 1$[51], where ρ is density, σ is surface tension, u is flow velocity and R is characteristic length), the droplet transfer volume (V_t) can be considered as an invariant in a microfluidic device.

Furthermore, the operational principle of the digital microfluidic meter-on-chip (DMC) has been depicted in detail in **Figs. 1a-d**. During the digitization process, a micro-nozzle generates a minute volume of fluid towards the downstream collecting reservoir under Laplace pressure[52]. As the droplet gradually approaches, the capillary force pulls the droplet and transfers the volume into the reservoir upon the immediate liquid contact[53]. We can further classify this process into three individual stages: 1) Emergence – the droplet first emerges from the nozzle, and the droplet gradually approaches the downstream liquid interface (**Fig. 1b**); 2) Coalescence – upon the liquid contact, a liquid bridge connects the droplet and the reservoir, establishing a continuous liquid path, equivalent to a closed-loop circuit in electronics (**Fig. 1c**); 3) Pinch-off – Following a brief period of capillary actions and force rebalance, the liquid bridge would spontaneously pinch off, equivalent to switching to an open-loop circuit, while a fixed amount of liquid is transferred to the reservoir (**Fig. 1d**). Under a continuous fluidic flow, this capillary process repeats itself. It is worth noting that the coalescence and pinch-off states during the discretization process can be detected either optically (as the structural digitizer can be made into a transparent device)[54] or electrically (as most fluids have much higher electrical conductivity than air[55]). **Fig. 1e** provides a close-up view of a transparent DMC prototype made from PDMS.

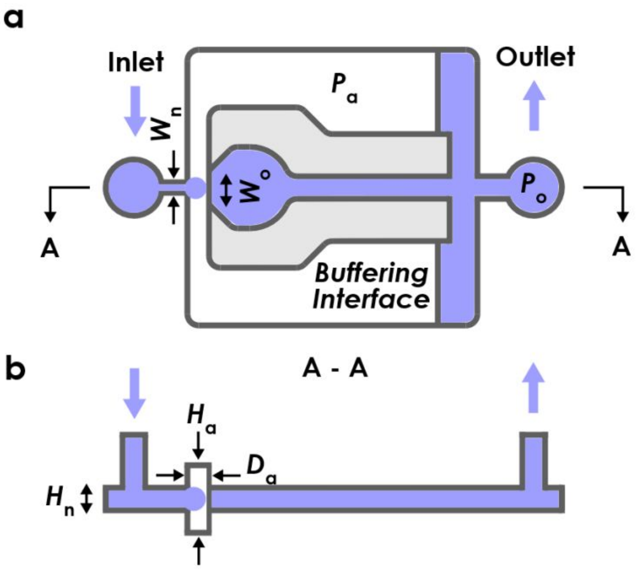

Fig. 2 Governing parameters in the DMC device. a) Top view and b) Slice view of the DMC device structural design.

As depicted in **Fig. 2**, the proposed DMC device consists of three main components: the micro-nozzle to generate the droplets and the downstream collecting reservoir, separated by an air-buffered chamber. The geometrical parameters of the micro-nozzle determine the droplet transfer volume (V_t), as predicted by the theory of capillarity-governed droplet dynamics[56]. In particular, the dimensions of the nozzle (W_n and H_n) together with the separation distance (D_a) control the droplet transfer volume. Therefore, the nozzle design with the deliberately chosen geometrical parameters can be used to adjust the volume resolution and sensitivity of the DMC devices. Furthermore, the air chamber plays two critical roles in microfluidic flowmetry, first permitting the discretization of continuous flow under capillarity, and second providing a buffering mechanism to stabilize the air-liquid interface at the collecting reservoir under the outlet pressure variations. Specifically, the air-buffered chamber has a different height (H_a) than that (H_n) of the nozzle and the reservoir. This would ensure that during the period of droplet formation, the droplet would not be interfered with the top and bottom surfaces of the air chamber. Furthermore, when the outlet pressure (P_o) increases, the pressure inside the air-buffered chamber (P_a) elevates accordingly as the air volume being compressed, i.e., $P_\mathrm{a} \approx P_\mathrm{o}$, especially when the curvature of the buffering air-liquid interface at the side air chamber is small. On the other hand, the pressure drop across the air-liquid absorbent interface at the collecting reservoir would remain negligible, i.e., $P_\mathrm{a} - P_\mathrm{o} \approx 0$ in quasi-static states (when the outlet pressure is not drastically changing). As a result, the surface tension force (along with Laplace pressure) remains unaltered at the droplet-forming interface, even when the outlet pressure has varied. Lastly, the droplet-collecting reservoir regulates the pinch-off of the droplet and the outflow of the transferred liquid from the micro-nozzle, which requires a stable and planar interface for consistent droplet coalescent processes with a constant transfer volume. This has been addressed by implementing a tapered-shape channel in the droplet-collecting zone as shown in **Fig. 2a** and optimizing the width (W_o) of the absorbent interface. Specifically, a nozzle design of the tapered shape with an acute angle reduces the tendency of the contact line to depin from the edges of the reservoir. This is because as depinning and moving towards downstream increases the surface area of the absorbent interface, it would result in rise of the overall surface energy and become thermodynamically unfavorable for systematic energy minimization[57]. On the other hand, the width of the absorbent interface controls the shape of the liquid bridge[50,58] particularly during the coalescence stage, and thus, it plays a critical role in the effective transfer of the droplet.

Materials and Methods

Fig. S1 illustrates the layer-by-layer fabrication of the DMC devices. The typical process started with the coating of a thin SU-8 3050 photoresist (MicroChem Corp.) on top of a 4 inch silicon wafer (UniversityWafer, Inc.) with a spin coater (Laurell Technologies Corporation), followed by the standard soft bake, UV light exposure with a mask aligner (ABM Inc.) and post-exposure bake to transfer the pattern of the DMC design from a high-resolution glass photomask (HTA Photomask) to the deposited photoresist. **Fig. S1a** shows the latent pattern image of the first layer after the post exposure bake. Next, a second layer of SU-8 with controlled thickness was spin-coated above the first layer, followed by the same process of baking and UV exposure to transfer a second pattern of the DMC design to the second layer of the photoresist, as shown in **Fig. S1b**. The two-layer SU-8 coated silicon wafer was then immersed in SU-8 developer to dissolve the unexposed (not cross-linked) photoresist and form a SU-8 master with three dimensional structures, as shown in **Fig. S1c**. In the subsequent step, PDMS elastomer (SYLGARD$^\mathrm{TM}$ 184, Dow Corning) was prepared by mixing the base and curing agent at a weight ratio of 10:1 and poured on top of the SU-8 master placed in a petri dish. After degassing in a desiccator, the petri dish containing the SU-8 master and PDMS was put in an oven set at 80°C to thermally cure the PDMS, as shown in **Fig. S1d**. After that, the PDMS mold was peeled off from the SU-8 master, depicted in **Fig. S1e**. Another piece of PDMS mold was prepared using the same method, and the inlets/outlets were made using a PDMS puncher (World Precision Instruments WellTech Rapid-Core 500 μm). These two identical layers were bonded together using a plasma cleaner (Harrick Plasma) to form the final DMC device illustrated in **Fig. S1e**. The two layers were carefully aligned under a microscope (Life Technologies EVOS XL) by adding a drop of ethanol in between, which is followed by heating up on a hotplate (Corning PC-620D) at 150°C for 4 hours to enhance the bonding strength and also recover the hydrophobicity of PDMS. It is worth mentioning that the dimensions of the nozzle are critical to the DMC metering system, and in practical skin wearable applications, these dimensions should be kept relatively unchanged. This issue can be addressed by adding a soft and flexible cushion layer between the DMC device and the skin. In such cases, the DMC device itself can be made more rigid, while the whole microfluidic wearable device is still kept flexible. Finally, by inserting 90° stainless steel needle (26 gauge, McMaster-Carr) and tubing in the inlets and outlets, the device is ready for testing.

A syringe pump (Harvard Apparatus 11 Pico Plus Elite) with a 1 mL glass syringe (Hamilton 1000 Series) was used to generate the preset flowrate for the characterization of the DMC, using 0.9 wt% saline as the working fluid. If the liquid composition varies, a calibration process can be conducted following the procedure mentioned here. First, DMC devices were primed with saline from the outlet, and then the inlet of the DMC was connected to the syringe for testing via a miniature tubing (Cole-Parmer Microbore PTFE Tubing, 305 μm ID x 762 μm OD). To determine the outlet pressure, a manometer (Sper Scientific) was connected to the inlet/outlet tubing of the DMC devices with a three-way stopcock (B. Braun Medical Inc.). To vary the outlet pressure, one port of the three-way connector was attached with an empty syringe filled up with air, and pressure can be adjusted by compressing the air inside the syringe. Both electrical and optical methods were used to detect the events of coalescence and pinch-off in the flow discretization process in DMC devices. A simple electrical circuitry driven by a DC power supply (BNC Model 1533) and a function generator (BNC Model 645) was used to detect the impedance change, as shown in **Fig. S2**, similar to the one reported in our previous work[45]. The output impedance signal was acquired by a DAQ board (National Instruments, USB-6210) at sampling rate at 1 and 10 kS/s and displayed with a LabVIEW interface[45]. To optically detect the discretization frequency, a smartphone (Sony Xperia XZ1) attached with a microscope (Omano Microscopes) was used to capture the dynamics of the droplets at a frame rate up to 960 fps. In addition, a high-speed camera (Phantom VEO-E 310L) connected with the microscope was used to record the detailed shape evolution of the droplets in the process of coalescence and pinch-off at frame rate over 10,000 fps. A MATLAB Canny function was used to detect the transient edge of the droplet in each captured frame, from which the frequency of flow discretization can be determined.

Results and Discussion

Based on the operational principle of the digital microfluidic meter-on-chip, we have first investigated the flow dynamics of the digitization process in the digital flowmetry using high-speed imaging. Secondly, we have evaluated three critical specifications in digital flowmetry, that is, volume resolution of digitization, device sensitivity and measurement range, by designing the geometrical parameters in DMC devices accordingly. Furthermore, two straightforward readout schemes, including electrical and optical detection, have been implemented and compared in detail. The influences of the air-buffered chamber have also been discussed.

Dynamics of the Digital Flowmetry

A series of high-speed microscopic images have been captured to elaborate the details during the three stages in the digitization process of the DMC device, that is emergence, coalescence and pinch-off, as introduced in Operating Principle. As shown in **Fig. 3**, throughout the entire process, the droplet is pinned effectively to the edge of the nozzle and the absorbent interface is pinned to the sharp edges of the collecting reservoir.

As discussed previously, the overall flowrate Q is correlated with the droplet transfer volume V_t and frequency of digitization f as follows and can be expanded: $Q = f \cdot V_\mathrm{t} = (V_\mathrm{c} - V_\mathrm{r})/(t_\mathrm{e} + t_\mathrm{b})$, at low flowrate ($We \ll 1$) conditions. As denoted in **Fig. 3**, V_c is the droplet volume at coalescence, V_r is the remained droplet volume after pinching off, and t_e and t_b denote for the duration of emerging and liquid bridging, respectively.

As shown in **Fig. 3a**, upon contact, the droplet coalesces with the liquid in the collecting reservoir. Once coalesced, a liquid meniscus neck forms (as shown in **Fig. 3b**) and expands, draining liquid from the droplet into the microchannel in the downstream. As can be seen, the liquid bridging status (t_b) lasts for approximately 1.6ms. As the geometries of the DMC are restricted to a microscale where the capillarity dominates, the duration of liquid bridging t_b is expected to be a liquid-specific geometric-determined constant in the low Weber number region[56,59].

As shown in **Fig. 3c**, immediately after the pinch-off, a pendant droplet remains pinned to the nozzle. In the capillarity-governed droplet dynamics, V_r is proportional to V_c[58,60]. The droplet forms a spherical shape under surface tension, from which its V_c can be geometrically determined. As a result, the droplet transfer volume $V_\mathrm{t} = V_\mathrm{c} - V_\mathrm{r}$ will become a liquid-specific geometric-determined constant, decoupled from the coming flowrates.

After the pinch-off of the liquid bridge, the droplet starts another cycle, emerging and approaching towards the absorbent interface, as shown in **Figs. 3d-e**. The duration of emerging (t_e) is approximately 13.3ms under the current device configuration and at a flowrate of 10μL/min. It is worth noting that t_e is flowrate-dependent. At a greater flowrate, the droplet will take a shorter time to reach the absorbent interface. As a result, the frequency of digitization (f) is approximately 67Hz at a flowrate of 10μL/min, given the flowrate-independent constant of t_b is 1.6ms. The corresponding video has been included in the **ESI**.

We have considered the influence of nozzle geometry in the droplet generation and selected the nozzle width as one of the most influential parameters in this study and the relevant experimental data have been reported in **Fig. 4B**. We have also considered the influence of the tapered angle of the nozzle. We have tried to use a straight nozzle design without any tapered angle and have discovered that it can result in wetting of the side walls of the nozzle, and thus, may lead to the failure of the operation after repetitive droplet digitization. As a result, we have switched to a tapered angle in the design of the nozzle to ensure that the advancing contact angle during droplet emerging is smaller than the critical angle, which prevents the side walls from wetting throughout the digitization process.

Characterizations of DMC Devices

The performance of a flow sensor can be specified with several parameters, including two of the most critical ones, specifically, device sensitivity and measurement range[61]. Moreover, in digital flowmetry, the volume resolution of digitization, in other words the droplet transfer volume, is also a crucial measure. Here, we have

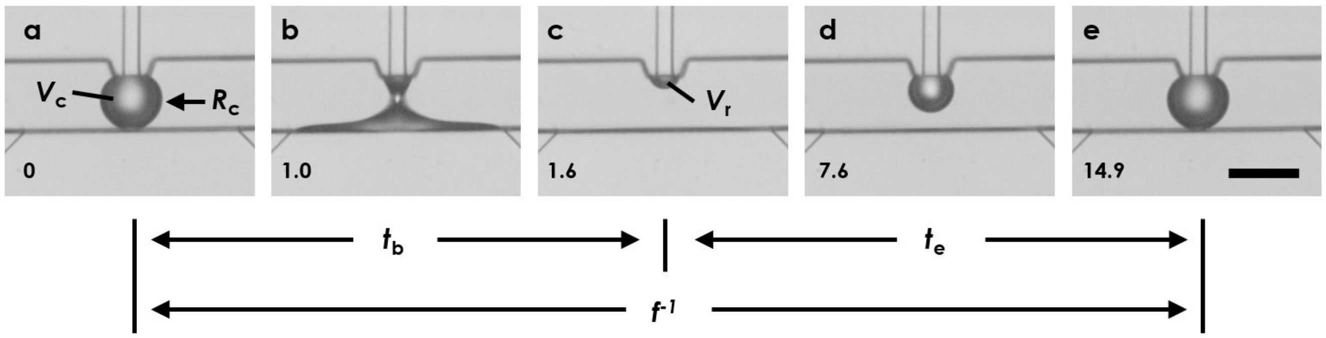

Fig. 3 High-speed images of the dynamic coalescence and pinch-off process at a flowrate of 10 μL/min, validating the three stages of emerging, coalescing and pinching off in DMC devices. Listed times are in milliseconds after onset of coalescence. The scale bar in the last frame is 200μm.

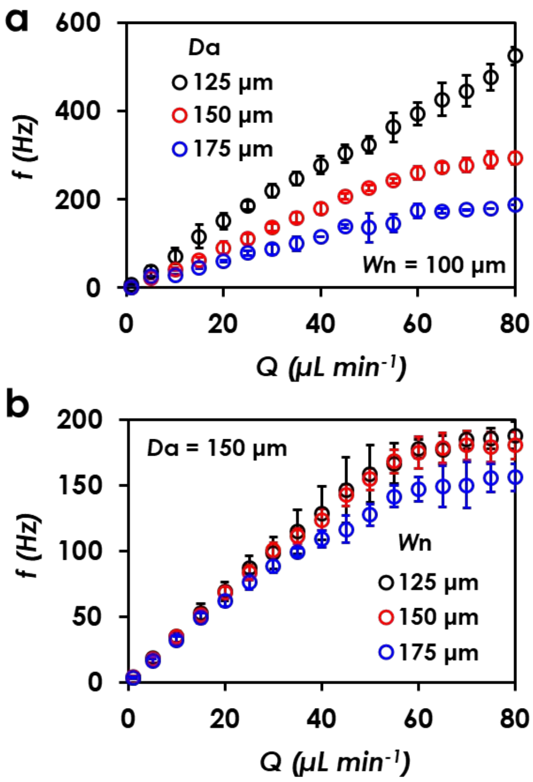

Fig. 4 Parametric study of DMC devices. Dependence of sensitivity on geometrical confinements including a) separation distance and b) nozzle width.

conducted parametric studies and will discuss these characteristic specifications of DMC devices in detail.

Device sensitivity and volume resolution: The sensitivity (S) in flowmetry is defined as the ratio between the measured sensor output and the given input flowrate[61]. In digital flowmetry, the device sensitivity should follow the defined frequency-to-flow relationship as: $S = f/Q = 1/V_\mathrm{t}$, inversely proportional to the droplet transfer volume V_t. Here we define V_t as the volume resolution in droplet flowmetry. It is worth noting that the volume resolution is different from the conventional concept of resolution in flowmetry, which is defined as the minimum detectable variation of input flow[61]. As aforementioned, under low flowrate conditions, V_t is proportional to the droplet volume at coalescence, V_c, which is only geometrically determined. As a result, V_t is a flowrate-independent constant under such conditions. However, when the flowrate is high and inertial force dominates over capillary force, V_t will become flowrate-dependent and can no longer be considered a constant. Since sensitivity S is inversely proportional to V_t, it is expected that under low flowrate conditions, S will also be a constant while under high flowrate conditions, S will be flowrate-dependent. **Fig. 4** shows the results of the dependence of sensitivity and volume resolution on flowrates and the geometrical dimensions, by varying the separation distances and nozzle sizes. For each DMC geometry, at least three devices have been fabricated and tested, from which the errors bars in **Fig. 4** indicate the average signal outputs and reflect the fabrication inconsistencies among different DMC devices.

Fig. 4a illustrates the frequency changes over a wide range of flowrates with different sizes of separation distances from 125μm to 175μm, given the nozzle width of 100μm and nozzle height of 150μm. It is worth mentioning that a parametric study of the nozzle depth has been conducted in this work, ranging from 100μm to 200μm. With a small depth of 100μm, the droplet digitization process is found inconsistent. On the other hand, with a large depth of 200μm, the fabrication process is challenging. As a result, a device depth of 150μm has been determined to use in all the relevant studies. As can be seen, under low flowrate conditions, the frequency is linearly proportional to the flowrates as expected. Thus, the sensitivity of the DMC devices, denoted as the slope rate, is approximately a constant. At high flowrate condition, however, the response of the DMC devices saturates, the sensitivity gradually drops, and the volume resolution degrades, due to the crossover from capillarity-governed flow regime to inertia-governed regime. As shown in **Fig. 4a**, a longer separation distance would result in a narrower linear measurement range. In another word, a smaller separation distance is more desirable for a wider range of flowrate assessments.

With the smallest separation distance of 125μm, the highest sensitivity of 6.59Hz/(μL/min) has been measured. This corresponds to the highest volume resolution (2.5nL), nearly two orders of magnitude higher than that of the previously reported (128nL) in the droplet flowmetry[46] for assessment of ultralow flowrates (at magnitude of 1μL/min). In comparison, as the separation distance is increased by 40% to 175μm, the sensitivity drops to 2.87Hz/(μL/min) and the corresponding volume resolution degrades to 5.8nL.

Here, we intend to determine the upper and lower boundaries to sensitivity and resolution, which are related to the droplet size. The viscosity force plays a critical role in setting up the upper boundary of the device sensitivity, by determining the minimal functional size of the droplet. As the droplet size scales down, the viscosity force becomes no longer negligible, potentially leading to complete coalescence, instead of pinch-off[60]. For the device configuration in **Fig. 4a**, it is experimentally determined that the gap distance of 100μm still results in the coalescence, and therefore, the smallest gap distance has been set at 125μm in this study. On the contrary, the lower boundary of sensitivity, related to the maximal droplet size, is mainly limited by geometrical confinements. Specifically, it should be avoided that the droplet be in physical contact with the ceiling or floor of the air chamber. This can be achieved by selecting an appropriate nozzle size with a proper separation distance, once the air chamber height is given. In this study, we have experimentally determined that a gap distance less than 175μm can avoid the issue.

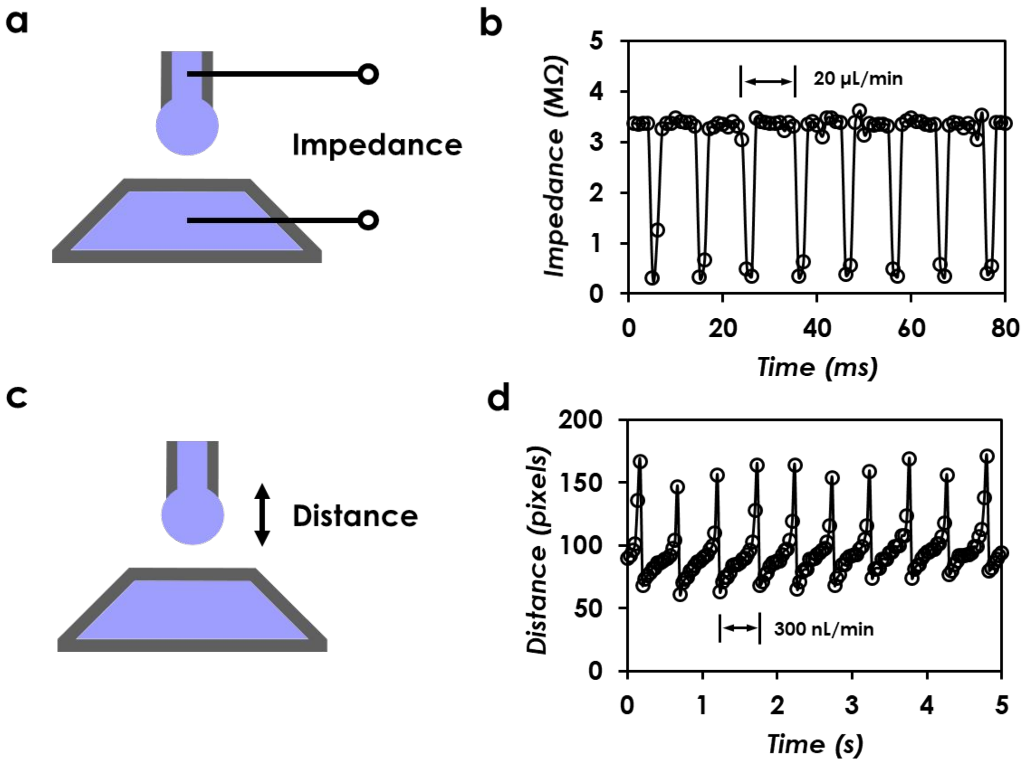

Fig. 5 Electrical and optical detection of flow discretization in DMC devices. a) Electrical detection of the digitization frequency. b) Electrical detection of the impedance in the process of coalescence and pinch-off. c) Optical detection of the digitization frequency. d) Optical detection of the tip distance of the emerging droplet.

Fig. 4b presents the variations of frequency changes over different nozzle widths ranging from 125μm to 175μm, provided the nozzle height of 150μm and separation distance of 150μm. It is found that nozzle widths greater than 175μm result in complete coalescence instead of pinch-off, while nozzle widths smaller than 125μm can lead to the detrimental wetting of the nozzle surrounding during the coalescence and pinch-off process. The variations of nozzle sizes result in similar trends in volume resolution and sensitivity. As can be seen in **Fig. 4b**, the smallest nozzle width results in the highest sensitivity of 3.16Hz/(μL/min) and the corresponding highest volume resolution is 5.3nL. As the nozzle width rises to 175μm, the device sensitivity drops to 2.65Hz/(μL/min) and the volume resolution reduces to 6.3nL. As shown in **Fig. 4b**, it is found that the sensitivity is relatively insensitive to the change of nozzle width under the current geometrical configurations.

Measurement range: As a convention, the maximum detectable flowrate ($Q_{\max}$) and the minimum detectable flowrate ($Q_{\min}$) are used to confine the measurement range in flowmetry.[61] As aforementioned, the sensitivity gradually drops at high flowrates. It is worth noting that the maximum flowrate $Q_{\max}$ for a flow sensor is typically defined at the point of the maximally permitted deviation of the sensitivity from the measured value in its linear range, which can be customarily pre-defined[61]. In our case, we have defined the maximally permitted deviation at 15%, from which $Q_{\max}$ can be determined accordingly. In addition, we define $f_{\max}$ as the corresponding maximum operational frequency at the flowrate of $Q_{\max}$.

As shown in **Fig. 4a**, $f_{\max}$ has been experimentally observed around 524Hz, given the shortest separation distance of 125μm, with the corresponding peak flowrate $Q_{\max}$ of approximately 80μL/min detected. Further increase in flowrate results in significant deviation and therefore the data is not included. The maximum frequency f_{max} has decreased to 177Hz at a longer separation distance of 175μm, while $Q_{\max}$ falls to 70 μL/min, lower than the one with the shortest separation distance. Similarly, as shown in **Fig. 4b**, when changing the droplet volume by tuning the nozzle width, the smallest nozzle width of 125μm results in the highest operational frequency $f_{\max}$ of 165Hz and the highest maximum flowrate $Q_{\max}$ of 50μL/min. As the nozzle width rises to 175μm, $f_{\max}$ reduces to 110Hz and $Q_{\max}$ remains approximately the same at 40μL/min.

In principle, at extremely high flowrates conditions ($t_{\mathrm{e}} \ll t_{\mathrm{b}}$), $f = 1/(t_{\mathrm{e}} + t_{\mathrm{b}})$ approaches to $f_{\max} \approx 1/t_{\mathrm{b}}$. Since t_{b} is directly related to the geometrical parameter as aforementioned, a smaller geometrical dimension leads to a shorter duration of bridging t_{b}. As a result, the maximum digitization frequency $f_{\max}$ will be higher for smaller geometrical dimensions. The experimental results are consistent with our predictions from the simplified analysis above. Therefore, the maximum flowrate $Q_{\max}$ can be determined in the targeted low Weber number region. On the other hand, the minimum detection flowrate, $Q_{\min}$, is mainly influenced by the Laplace pressure barrier (

$\Delta P = 2\sigma/R$), which is the threshold pressure that the droplet needs to emerge from the nozzle, moving through the hemispherical limit[57]. Given a nozzle with a hydraulic radius (R) of 50μm, the maximum pressure required for pure water is approximately 2.9kPa at a room temperature[50]. The lowest detectable flowrate is measured approximately 150nL/min (using 1Hz as the self-defined practically useful minimum digitization frequency), under the current design parameters. It is worth mentioning that the length of the nozzle matters indeed, as it contributes to the overall flow resistance. For wearable applications without an external drive, the channel size and nozzle dimensions should be adjusted to ensure minimal pressure drop throughout the droplet generation process.

In addition, the dynamic response of the DMC devices has also been characterized. Flowrates increased from 5μL/min to 15μL/min and decreased from 15μL/min to 5μL/min are both studied for the DMC devices with W_n of 100μm and D_a of 150μm, and the corresponding response time are determined to be approximately 200ms and 175ms, respectively, as shown in **Fig. S5**.

We expect that the droplet transfer volume will change if the viscosity and surface tension of the liquid change. The DMC devices might fail to work when the liquid viscosity is high, or the surface tension is low[56,60]. When the composition changes or a detergent is added, while the overall liquid properties still stay within the proper ranges, a calibration procedure needs to be conducted by the operators following the procedure mentioned in the section of "Materials and Methods".

Electrical and Optical Measurement of the Digitization Process

As aforementioned, in digital flowmetry, the frequency of digitization f is linearly proportional to the interested flowrate Q at low flowrate conditions. Therefore, the precise measurement of f is of crucial importance in digital flowmetry. In this study, the frequency range of digitization is up to 524Hz. Here, we have demonstrated that both simple electrical and non-contact optical detection methods (as illustrated in **Fig. 5a** and **Fig. 5c**, respectively) can be applied to determine such a frequency of digitization and compute the corresponding flowrates.

In the electrical detection scheme, two electrodes can be inserted into the upstream of the nozzle and downstream of the collecting reservoir, respectively, as shown in **Fig. 5a**. Using a simple signal acquisition system as introduced in the previous work[45], the electrical impedance across the two electrodes can be measured with a high temporal resolution. **Fig. 5b** exhibits the measured electrical impedance at a flowrate of 20μL/min at an electrical sampling frequency of 1kHz. Using an electrically conductive saline solution as the working fluid, the overall impedance is approximately 3.5MΩ in the open-circuit state, which drastically drops below 0.5MΩ in the closed-loop scenario upon the formation of the liquid bridge, following the droplet coalescence. The droplet digitization frequency can be deducted from the time interval between the two adjacent fluctuations of the measured impedance, which has been found approximately 100Hz. At a higher sampling frequency of 10kHz, the electrical detection method would enable us to measure the coalescence and pinch-off process at digitization frequency of 524Hz precisely (with the corresponding flowrate of 80μL/min). As the high-resolution electrical measurements would lead to high accuracy and precision in the assessments of frequency of digitization, the electrical detection approach has therefore been preferred in the characterization and parametric studies of the DMC devices.

One fundamental and unique feature of digital flowmetry is that the output signal is the frequency (of digitization), and this has enabled us to apply a non-invasive and non-contact optical detection readout scheme to the DMC devices. In the optical detection scheme shown in **Fig. 5c**, the interfacial separation between the emerging droplet and the collecting reservoir can be optically recorded and mathematically extracted. The change of the separation distance from the tip of the droplet to the baseline of the nozzle can be utilized to calculate the frequency of the periodic flow discretization[62]. **Fig. S3** illustrates a series of recorded snapshots of the entire droplet emergence, coalescence and pinch-off process at the flowrate of 300nL/min, captured by a consumer cellphone camera (Sony Xperia XZ1) at 30 frame/sec. The transient distance (in pixels) is determined by an edge detection algorithm enabled by MATLAB Canny function. By comparison with the high-speed video, we find that the peaks are formed near the instant of coalescence. The consistency and periodicity of the tip distance in **Fig. 5d** demonstrate the effectiveness of our data analysis method. It is worth noting that the time resolution of the optical detection is limited by the highest recording frame rate of the phone camera. The results shown in **Fig. 5d** are recorded at 30fps (equivalent time resolution around 33ms), and the digitization frequency of approximately 2Hz has been successfully detected. Using the advanced off-the-shelf smartphone, a frame rate of 960 fps (equivalent time resolution around 1ms) can be achieved. As measured, the current optical detection method is feasible of measuring DMC frequency up to 200Hz (equivalent to the maximum flowrate of 80μL/min at the current configuration as shown in **Fig. 4b**) using a commercial smartphone. This optical measurement approach would eliminate the need of developing a custom high-precision measurement device by directly using a commercial mobile phone, while still achieving an ultrahigh flowrate measurement (up to 80μL/min).

Influences of the Air-Buffered Chamber

As aforementioned in Operating Principle, the air-buffered chamber (ABC) is included in the DMC design to stabilize the air-liquid interface at the collecting reservoir under the outlet pressure variations. In the original symmetrical air chamber design, as shown in **Figs. 4a-b**, once the outlet pressure increases, the buffering interface on one side of the chamber would move toward the nozzle and compress the air chamber. As a result, the interfacial pressure difference remains unaltered. However, the interface at the other chamber would become stagnant, because the Laplace pressure barrier (similar as in the capillary valves[63]) at the junction of the air chamber and the collecting reservoir will prevent the liquid from moving towards the air chamber. To remove such a design redundancy, we have implemented an asymmetrical design, as shown in **Figs. S4c-d**, in which the whole volume of the air chamber can be effectively utilized, and the overall footprint of the device can be significantly reduced (by approximately 1/2 of the symmetrical configuration). Another important consideration is the maximum outlet pressure the ABC can handle. Due to the stagnant air-liquid interface in one side of the symmetrical design, the maximum outlet pressure of the ABC has to be less than 2 atm. Whereas the maximum outlet pressure follows $P_{\text{a\_max}} = (1 + V_{\text{a}}/V_0)P_0$ in of the asymmetric design, where V_{a} and V_{o} define the buffering and dead volume zones of the ABC, respectively. In another word, if the dead volume V_0 is designed to be considerably smaller than the buffering volume V_{a}, the maximum permittable outlet pressure of the DMC devices can be substantially increased. The detailed derivations on the maximum outlet pressure have been included in the **ESI**.

Secondly, we have further studied the influence from the outlet pressure variations on droplet transfer volume, and consequently, the flowrate measurement. As shown in **Fig. S4e**, the droplet transfer volume V_{t} (3.5nL) is experimentally found independent from the outlet pressure, which also validates that the buffering and stabilizing functions of the air chamber as aforementioned. In brief, the ABC, by decoupling the droplet transfer volume from the outlet pressure fluctuations, simplifies the device calibration and plays an important role in improving the flow measurement accuracy and applicability of the DMC device.

It is worth mentioning that the device dimensions have no direct influence on the droplet digitization process, as long as the width of the buffering interface is larger than that of the absorbent interface. However, the larger dimensions would reduce the Laplace pressure of the buffering interface, and thus, make the interface easier to move and more responsive to variations of the outlet pressure, at the cost of increasing the overall dimensions of the DMC devices.

Demonstration

To demonstrate the integrability of the proposed DMC sensors for microfluidics applications, an array of four DMC devices is designed and embedded with a classic Christmas-tree-like gradient generator widely used in the microfluidic community[64]. The DMC can then be used to monitor the transient flowrate variations in each of the four downstream branch channels, as shown in **Fig. 6a**. The theoretical flowrate in each branch channel can be calculated using fluidic and electric circuit analogy[65]. The coming flow injection is controlled by two individual syringe pumps, from which the dynamic responses of the DMC devices has been measured. In the first setting, the two inlets are both set at a flowrate of 90µL/min. The theoretical flowrates are 40µL/min for outlets 1 and 4, and 50µL/min for outlets 2 and 3. **Fig. 6b** shows the recorded flowrates in each of the four DMC devices. As expected, the two DMC devices in the center and the two DMC devices on each side captured approximately the same flowrates at a steady state, respectively. The measured flowrates are 39.2, 44.7, 44.8 and 36.9µL/min in each of the four branch channels. The total flowrate in the four channels is 165.6µL/min, deviated within 8% from the theoretical value of 180µL/min. In the second case, the two inlets are set at flowrates of 90µL/min and 50µL/min, respectively. The theoretical flowrate distribution in the four outlets are approximately 32, 40, 38 and 30 µL/min. The distribution of flowrates is varied in the four channels and it has been successfully detected by the embedded DMC sensors. The total flowrate in the four channels is 134.9µL/min, within 4% deviated from the theoretical value of 140µL/min. The experimentally measured flowrates are 31.4, 43.0, 33.8 and 26.7µL/min in each branch channel, respectively. The deviations in each of the four channels are within 10% of the theoretical values. Importantly, in addition to the intriguing high sensitivity, high volume resolution, high compatibility and adaptivity, facile fabrication process, simple (non-contact) readout, battery-free passive working mechanism, wide

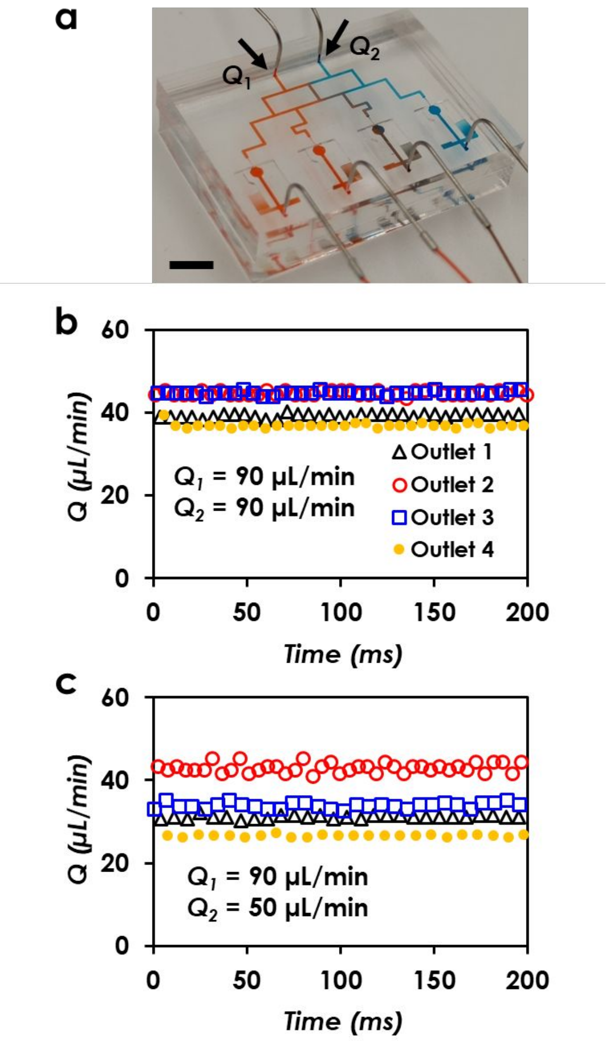

Fig. 6 Demonstration of embedded DMC devices in a microfluidic Christmas-tree-like gradient generator. a) Prototype of an array of four DMC devices. The scale bar is 5mm. Real-time flowrate measurement with two inlets at the b) same flowrate and c) different flowrates.

measurement range, the DMC devices can also offer equivalent or better performance in terms of measurement accuracy (5% to 10%), compared with the commercial counterparts. The current deviation from theoretical values is most likely caused by the laboratory fabrication inconsistency among different sets of the DMC devices, where the misalignment can present a major issue during the manual fabrication process[66]. It is expected that further improvement in alignment can lead to a higher accuracy. In conclusion, the measurement results have shown the ability of the DMC system to provide the first in situ, multiplexed, and real-time digital detection of liquid flow embedded in microfluidic devices.

Conclusions

In this paper, we have first presented a readable and embeddable microflow measurement method, referred to as microfluidic digital meter-on-chip (DMC) with a simple device architecture and tunable sensitivities for on-chip and local microflow assessments in conventional PDMS-based microfluidic devices. The digital flowmetry principle utilizes capillarity-governed flow discretization to digitizing continuous flow into uniform and countable individual units of transferred liquid volume. Under small flowrates, inertial force can be neglected, and it is found that the discretization process is dominated by surface tension forces and geometrical configurations, and therefore, the unit droplet transfer volume is identical and can be decoupled from coming flowrates. A theoretical model has been proposed to correlate the governing geometrical parameters (nozzle size and separation distance) with the device sensitivity and volume resolution. The DMC devices offer several distinct advantages over the existing counterparts: (1) ultrahigh flow-to-frequency sensitivity (6.59 Hz/(μL/min)) and volume resolution (droplet transfer volume down to 2.5 nL), over 50 times the highest reported value[46] with similar digital principle (128nL) targeting ultralow flowrates (at magnitude of 1μL/min), (2) highly compatible and adaptive to conventional PDMS-based microfluidic devices enabled by the facile layer-by-layer fabrication process, (3) simple frequency readout enabled by the two digital sensing (electrical and non-contact optical) mechanisms, leading to the potential of using non-contact and wireless optical detection scheme, and eliminating any bulky off-chip control and communication equipment, (4) passive flow discretization principle, and thus no external power (battery) required, (5) wide flowrate measurement range at least covering from 80μL/min down to 150nL/min (over 100 times smaller than the reported similar digital flowmetry[46] at the same time scale) under the current device configuration. Benefiting from its simple device architecture and adaptability, the versatile DMC technology can be potentially deployed in various microfluidic and nanofluidic applications in drug delivery and biochemical analysis as a promising candidate for the next-generation high-accuracy microflow and nanoflow measurements.

Author contributions

T.P. and Z.F. conceived the idea and designed the experiments. Z.F. led the experimental testing. Z.F. led the development of theoretical model. Z.F. and T.P. contributed to data analysis and interpretation. Z.F. led the structural design of the device with assistance from Y.D. Y.D. led the fabrication of the devices with assistance from Z.F. Z.F. led the high-speed imaging and optical detection, with assistance from F.W. Y.D. led the circuit buildup and code development for electrical detection with assistance from Z.F. and Z.Z. H.W. and Z.W. provided guidance and advice on microfluidic flowmetry. Z.F. and T.P. wrote the paper and all authors provided feedback. T.P. supervised the study.

Conflicts of Interest

There are no conflicts to declare.

Acknowledgements

This research work was supported in part by NIEHS UC Davis Superfund Project 5P42ES004699-30 and USDA-NIFA Grant 2018-67017-28116. The authors would like to acknowledge Dr. Yahui Yang for his valuable discussion.

References

1 R. A. Peterfreund and J. H. Philip, *Expert Opin. Drug Deliv.*, 2013, **10**, 1095–1108.
2 C. M. T. Sherwin, N. J. Medlicott, D. M. Reith and R. S. Broadbent, *Arch. Dis. Child.*, 2014, **99**, 590–594.
3 B. Ziaie, A. Baldi, M. Lei, Y. Gu and R. A. Siegel, *Adv. Drug Deliv. Rev.*, 2004, **56**, 145–172.
4 Y.-C. Hsieh and J. D. Zahn, *Sensors Actuators B Chem.*, 2005, **107**, 649–656.
5 N. . Nguyen, *Flow Meas. Instrum.*, 1997, **8**, 7–16.
6 S. Silvestri and E. Schena, *Micromachines*, 2012, **3**, 225–243.
7 J. T. W. Kuo, L. Yu and E. Meng, *Micromachines*, 2012, **3**, 550–573.
8 D. A. Czaplewski, B. R. Ilic, M. Zalalutdinov, W. L. Olbricht, A. T. Zehnder, H. G. Craighead and T. A. Michalske, *J. Microelectromechanical Syst.*, 2004, **13**, 576–585.
9 Y. Gong, Q. Liu, C. Zhang, Y. Wu, Y. Rao and G. Peng, *IEEE Photonics Technol. Lett.*, 2015, **27**, 2508–2511.
10 A. S. Nezhad, M. Ghanbari, C. G. Agudelo, M. Packirisamy, R. B. Bhat and A. Geitmann, *IEEE Sens. J.*, 2013, **13**, 601–609.
11 V. Lien and F. Vollmer, *Lab Chip*, 2007, **7**, 1352.
12 N. Noeth, S. S. Keller and A. Boisen, *J. Micromechanics Microengineering*, 2011, **21**, 015007.
13 M. Sadegh Cheri, H. Latifi, J. Sadeghi, M. Salehi Moghaddam, H. Shahraki and H. Hajghassem, *Analyst*, 2014, **139**, 431–438.
14 R. Monge, J. Groenesteijn, D. Alveringh, R. J. Wiegerink, J. Lötters and L. J. Fernandez, *Sensors Actuators, B Chem.*, 2017, **241**, 744–749.
15 J. C. Lötters, T. S. J. Lammerink, J. Groenesteijn, J. Haneveld and R. J. Wiegerink, *Micromachines*, 2012, **3**, 194–203.
16 W. Sparreboom, J. van de Geest, M. Katerberg, F. Postma, J. Haneveld, J. Groenesteijn, T. Lammerink, R. Wiegerink

and J. Lötters, *Micromachines*, 2013, **4**, 22–33.

17 J. Groenesteijn, R. G. P. P. Sanders, R. J. Wiegerink and J. C. Lotters, in *2016 IEEE 29th International Conference on Micro Electro Mechanical Systems (MEMS)*, IEEE, 2016, vol. 2016-Febru, pp. 193–196.

18 A. Kuoni, R. l Holzherr, M. Boillat and N. F. de Rooij, *J. Micromechanics Microengineering*, 2003, **13**, S103–S107.

19 M. S. Cheri, H. Shahraki, J. Sadeghi, M. S. Moghaddam and H. Latifi, *Biomicrofluidics*, 2014, **8**, 054123.

20 J. Collins and A. P. Lee, *Lab Chip*, 2004, **4**, 7–10.

21 J. Wu and W. Sansen, *Sensors Actuators, A Phys.*, 2002, **97–98**, 68–74.

22 H. Berthet, J. Jundt, J. Durivault, B. Mercier and D. Angelescu, *Lab Chip*, 2011, **11**, 215–223.

23 E. Meng, P.-Y. Li and Y.-C. Tai, *Sensors Actuators A Phys.*, 2008, **144**, 18–28.

24 M. H. Zarifi, H. Sadabadi, S. H. Hejazi, M. Daneshmand and A. Sanati-Nezhad, *Sci. Rep.*, 2018, **8**, 139.

25 J. Chen, H. Guo, J. Zheng, Y. Huang, G. Liu, C. Hu and Z. L. Wang, *ACS Nano*, 2016, **10**, 8104–8112.

26 G. M. Whitesides, *Nature*, 2006, **442**, 368–373.

27 E. K. Sackmann, A. L. Fulton and D. J. Beebe, *Nature*, 2014, **507**, 181–9.

28 S.-Y. Teh, R. Lin, L.-H. Hung and A. P. Lee, *Lab Chip*, 2008, **8**, 198.

29 N.-T. Nguyen, X. Huang and T. K. Chuan, *J. Fluids Eng.*, 2002, **124**, 384.

30 D. J. Laser and J. G. Santiago, *J. Micromechanics Microengineering*, 2004, **14**, R35–R64.

31 A. Nisar, N. Afzulpurkar, B. Mahaisavariya and A. Tuantranont, *Sensors Actuators B Chem.*, 2008, **130**, 917–942.

32 A. K. Au, H. Lai, B. R. Utela and A. Folch, *Micromachines*, 2011, **2**, 179–220.

33 K. W. Oh and C. H. Ahn, *J. Micromechanics Microengineering*, 2006, **16**, R13–R39.

34 A. Y. Fu, C. Spence, A. Scherer, F. H. Arnold and S. R. Quake, *Nat. Biotechnol.*, 1999, **17**, 1109–1111.

35 D. Di Carlo, D. Irimia, R. G. Tompkins and M. Toner, *Proc. Natl. Acad. Sci. U. S. A.*, 2007, **104**, 18892–7.

36 H. A. Stone, A. D. Stroock and A. Ajdari, *Annu. Rev. Fluid Mech.*, 2004, **36**, 381–411.

37 A. S. Utada, E. Lorenceau, D. R. Link, P. D. Kaplan, H. A. Stone and D. A. Weitz, *Science (80-.).*, 2005, **308**, 537–541.

38 G. Schneider, *Nat. Rev. Drug Discov.*, 2017, 1994.

39 E. Kjeang, N. Djilali and D. Sinton, *J. Power Sources*, 2009, **186**, 353–369.

40 J. K. Nunes, S. S. H. Tsai, J. Wan and H. A. Stone, *J. Phys. D. Appl. Phys.*, 2013, **46**, 114002.

41 P. Zhu and L. Wang, *Lab Chip*, 2017, **17**, 34–75.

42 R. Attia, D. C. Pregibon, P. S. Doyle, J.-L. Viovy and D. Bartolo, *Lab Chip*, 2009, **9**, 1213.

43 Y.-J. Liu, J.-Y. Yang, Y.-M. Nie, C.-H. Lu, E. D. Huang, C.-S. Shin, P. Baldeck and C.-L. Lin, *Microfluid. Nanofluidics*, 2015, **18**, 427–431.

44 N. MacGillivray, *J. Infect. Prev.*, 2009, **10**, S3–S6.

45 Y. Yang, S. Xing, Z. Fang, R. Li, H. Koo and T. Pan, *Lab Chip*, 2017, **17**, 926–935.

46 J. Francis, I. Stamper, J. Heikenfeld and E. F. Gomez, *Lab Chip*, 2019, **19**, 178–185.

47 X. Li, Y. Mao, Z. Zhu, Y. Zhang, Z. Fang, D. Wu, H. Ding, T. Pan, B. Li and J. Chu, *Microfluid. Nanofluidics*, 2019, **23**, 102.

48 M. R. Hillman, *J. Med. Eng. Technol.*, 1989, **13**, 166–176.

49 F. C. Flack and T. D. Whyte, *J. Clin. Pathol.*, 1975, **28**, 510–512.

50 P.-G. de Gennes, F. Brochard-Wyart and D. Quéré, *Capillarity and Wetting Phenomena*, 2004.

51 B. Ambravaneswaran, H. J. Subramani, S. D. Phillips and O. A. Basaran, *Phys. Rev. Lett.*, 2004, **93**, 034501.

52 S. Barkley, S. J. Scarfe, E. R. Weeks and K. Dalnoki-Veress, *Soft Matter*, 2016, **12**, 7398–7404.

53 J. D. Paulsen, *Phys. Rev. E*, 2013, **88**, 063010.

54 S. T. Thoroddsen, T. G. Etoh and K. Takehara, *Annu. Rev. Fluid Mech.*, 2008, **40**, 257–285.

55 A. Witten, *Handbook of Geophysics and Archaeology*, Routledge, 2017.

56 S. T. Thoroddsen and K. Takehara, *Phys. Fluids*, 2000, **12**, 1265–1267.

57 J. Berthier and K. A. Brakke, *The Physics of Microdroplets*, 2012.

58 F. BLANCHETTE and T. P. BIGIONI, *J. Fluid Mech.*, 2009, **620**, 333.

59 S. T. THORODDSEN, K. TAKEHARA and T. G. ETOH, *J. Fluid Mech.*, 2005, **527**, 85–114.

60 F. Blanchette and T. P. Bigioni, *Nat. Phys.*, 2006, **2**, 254–257.

61 P. Bruschi and M. Piotto, *Micromachines*, 2012, **3**, 295–314.

62 C. Clanet and J. C. Lasheras, *J. Fluid Mech.*, 1999, **383**, 307–326.

63 M. Zimmermann, P. Hunziker and E. Delamarche, *Microfluid. Nanofluidics*, 2008, **5**, 395–402.

64 X. Wang, Z. Liu and Y. Pang, *RSC Adv.*, 2017, **7**, 29966–29984.

65 K. W. Oh, K. Lee, B. Ahn and E. P. Furlani, *Lab Chip*, 2012, **12**, 515–545.

66 A. Rotem, A. R. Abate, A. S. Utada, V. Van Steijn and D. A. Weitz, *Lab Chip*, 2012, **12**, 4263.

Table of Contents Entry

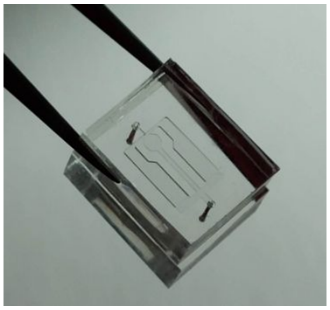

On-chip digital microfluidic flowmetry can be designed and incorporated in standard microfluidic devices for high-precision multiplexed microflow measurements.